ChemElectroChem

Research Article
doi.org/10.1002/celc.202400191

Chemistry Europe
European Chemical Societies Publishing

www.chemelectrochem.org

Photoelectrocatalytic Water Splitting by Conformal Copper-Oxide on Hematite Nanostructures: Dependence on Surface-States

Tímea Benkó,*[a] Shaohua Shen,[b] Miklós Németh,[a] Dávid Lukács,[a] Yufei Xu,[b] Irfan Khan,[a] Zsolt Czigány,[c] Zsolt Endre Horváth,[c] Zoltán Kovács,[c] Jinzhan Su,[b] and József Sándor Pap*[a]

Understanding the pivotal role of surface co-catalysts is paramount in the strategic design of forthcoming photoelectrodes. However, the nuanced impacts of co-catalysts remain elusive, particularly in promoting the water oxidation reaction on hematite, especially in connection to surface states denoted as S1 (higher energy) and S2 (lower energy). For this purpose, we tailored two isomorphous hematite nanoarrays with a thin layer of amorphous copper oxide (CuOx), composed of a blend of Cu(I) and Cu(II) species, *via* a soft electrodeposition technique. Remarkably, we discovered that in pristine hematite (**α-Fe_2O_3**), the S2 state played a pivotal role in activating the CuOx adlayer for water oxidation. At lower external biases (approximately 0.9–1.1 V_{RHE}), CuOx served as charge reservoir in equilibrium with the S2 state. Notably, beyond 1.1 V_{RHE}, where the high-energy holes of the S1 state became available, CuOx was activated indirectly through the equilibrium with the S2 state, and a pronounced enhancement in photocurrent was observed. Conversely, in the case of Ti-doped hematite (**Ti:α-Fe_2O_3**) devoid of the S2 state, the presence of CuOx resulted in a decline in charge transfer efficiency. Instead of facilitating water oxidation, CuOx adversely affected the S1 surface sites and reduced the charge carrier density in **Ti:α-Fe_2O_3**.

Introduction

Hematite (α-Fe_2O_3) is an environmentally benign and highly cost-efficient material that is worth consideration as photoanode in photoelectrochemical (PEC) water splitting devices. The band gap energy of α-Fe_2O_3 (2.0–2.2 eV) allows photoexcitation in the visible range, and the generated valence band holes (V_{BE} = 2.4–2.7 eV) are strong enough oxidizers to carry out the oxygen evolution reaction (OER, $2H_2O \rightarrow O_2 + 4H^+ + 4e^-$, 1.23 eV_{RHE}) on thermodynamic grounds.[1–3] However, inherent limitations such as poor electrical conductivity of 10^{-14} to 10^{-8} S cm^{-1},[4] typically high density of surface states, short hole lifetime of $<$10 ps and sluggish kinetics for the OER at the electrode/electrolyte interface limit catalytic potential.[1]

The performance deficit of α-Fe_2O_3 in water splitting can be improved by different strategies. Current research efforts are primarily focused on morphology control, element doping, the application of co-catalysts, surface modifications, heterojunction design, or the combinations thereof.[1,2,5–25] In this context, the chemical nature of intermediate surface states (SSs), their behavior under various conditions and role in the OER, on α-Fe_2O_3 made with a specific method is relevant to improvements.[2,26–28] One possibility to enhance the catalytic performance of SSs is elemental doping.[29,30] Lately, titanium was found effective as dopant to generate new electronic states within the bandgap that can serve as electron traps or facilitators of charge transfer processes.[31,32] Ti-doped hematite (Ti:α-Fe_2O_3) exhibits increased surface reactivity compared to its pristine counterpart, attributed to the formation of hydroxyl groups on the surface and better charge separation.[33] Importantly, doping can be done by the simple and scalable hydrothermal method providing α-Fe_2O_3 nanoarrays that are size-optimized for better charge carrier utilization.[29]

Considerable attention is paid to overcoming the charge transfer energy barrier by introducing finely dispersed co-catalyst nanoparticles, or thin co-catalyst layers on nanostructured α-Fe_2O_3.[1,2,5] The latter approach facilitates modifications conformal with the original morphology, thus projects the scalable fabrication of economical electrodes. In contrast to dopants, surface co-catalysts may reduce charge recombination, passivate the SSs, form heterojunctions for banding and charge separation, collect and store holes, but most importantly, provide new catalytic sites for the OER.[2] The alternative

[a] Dr. T. Benkó, M. Németh, Dr. D. Lukács, Dr. I. Khan, Dr. J. Sándor Pap
Surface Chemistry and Catalysis Department
HUN-REN Centre for Energy Research
1121 Budapest, Konkoly-Thege Miklós út 29–33, Hungary
E-mail: timea.benko@ek.hun-ren.hu
pap.jozsef@ek.hun-ren.hu

[b] Dr. S. Shen, Dr. Y. Xu, Dr. J. Su
State Key Laboratory of Multiphase Flow in Power Engineering (MFPE)
International Research Center for Renewable Energy (IRCRE)
Xi'an Jiaotong University, Xi'an, Shaanxi 710049, China

[c] Dr. Z. Czigány, Dr. Z. Endre Horváth, Dr. Z. Kovács
Institute of Technical Physics and Materials Science
HUN-REN Centre for Energy Research
1121 Budapest, Konkoly-Thege Miklós út 29–33, Hungary

Supporting information for this article is available on the WWW under https://doi.org/10.1002/celc.202400191

pathways for charge transfer at these new sites are expected to boost the OER effectively compared to the intrinsic SSs of hematite. However, considering the diverse possibilities, understanding the competitive *vs.* cooperative function of co-catalysts beside the SSs is vital for the efficient design of forthcoming photoanodes.

While IrO_2 has high efficiency as OER co-catalyst,[34,35] ongoing efforts aim at more cost-effective and available alternatives to allow large-scale application. Non-precious metal oxides, such as cobalt phosphate,[36–41] cobalt oxide,[42–45] iron oxyhydroxide,[46,47] and various mixed-metal oxides like nickel-iron oxide[48,49] and cobalt-iron oxide,[50] have emerged as promising substitutes, given their durability, wide accessibility, affordability, and resistance to chemical corrosion even under highly alkaline conditions. It can be asserted that hematite photoanodes loaded with non-noble metal co-catalysts hold great potential for making PEC water splitting a viable and scalable technology.

Copper oxide-based catalysts are known for their high activity in electrocatalytic OER,[41–53] but their utilization in PEC water oxidation is relatively rare. Semiconductive ad-layer of CuO has been reported to enhance the efficiency of α-Fe_2O_3 by forming a heterojunction,[54,55] yet, its use as a co-catalyst has not been clarified so far. In an earlier study, we reported an electrodeposition method for the uniform coating of hematite with a mixed, amorphous $CuO/Cu_2O/Cu(OH)_2$ (CuOx) using an environmentally benign and cost-efficient Cu-oligopeptide complex.[56] In this study, we introduce α-Fe_2O_3 and Ti:α-Fe_2O_3 isomorphous nanoarray photoanodes, modified with an ultra-thin, amorphous CuOx layer as putative co-catalyst in a morphology-preserving way. Importantly, the α-Fe_2O_3 and Ti:α-Fe_2O_3 anodes (**α-Fe_2O_3** and **Ti:α-Fe_2O_3**, respectively) are prepared in a scalable way on titanium sheets and their modification with CuOx is also convenient. The performance of hematite is strongly influenced by its surface state properties and known to be sensitive to the intimate contact with the co-catalyst.[57,58] Therefore, we compare pristine α-Fe_2O_3 and Ti:α-Fe_2O_3 photoanodes, with and without CuOx, in order to explore how this putative co-catalyst interacts with different SSs.

Results and Discussion

Structure and Composition of the Electrodes

Our aim was to grow arrays of hematite nanorods, oriented vertically to a conductive substrate – Ti sheet – that was practical to handle and scale according to needs, instead of the typical tin oxide semiconductive substrates more generally used in literature.[7,27,33] The size- and shape-optimized nanoarray arrangement was found crucial for the collection of photo-generated electrons and the charge migration allowing the photogenerated holes to reach the electrolyte interface efficiently, facilitating the water oxidation and further increasing PEC efficiency.[29] Note that contact optimization between hematite nanoarrays and Ti that could further enhance the achieved photocurrent was out of the scope of the present study.

The **α-Fe_2O_3** and **Ti:α-Fe_2O_3** nanoarrays were grown on Ti substrates *via* an aqueous solution approach based on Vayssieres' method.[1,59,60,61] In our earlier study,[56] the pre-catalyst **Cu–GGG** (Cu complex of Triglycine, H_3GGG)[62] resulted in excellent electrocatalytic performance under heterogeneous conditions in OER due to the formation of CuOx. Therefore, in this work, the bare **α-Fe_2O_3** photoanode was modified with CuOx (named as **CuOx/α-Fe_2O_3**) by the electrodeposition of **Cu–GGG** in borate buffer at pH 9.2 (see details in Figure S1). The same procedure was followed to prepare CuOx-modified **Ti:α-Fe_2O_3** electrode, named as **CuOx/Ti:α-Fe_2O_3**.

Bulk X-ray diffraction (XRD) analysis of the **α-Fe_2O_3**, **CuOx/α-Fe_2O_3** and **CuOx/Ti:α-Fe_2O_3** samples clearly confirmed the presence of the **α-Fe_2O_3** phase, with no detectable traces of CuOx phases (XRD spectra of the samples are shown in Figure S2). The absence of any Cu-containing crystalline phases in the XRD pattern strongly indicates the amorphous character of the CuOx ad-layer, although XRD as a bulk technique is not decisive in the case of identifying thin layers of only a few nanometers thick (see the detailed analysis by XPS and HAADF below). Top-view images by scanning electron microscopy (SEM) confirmed that the morphology of the **α-Fe_2O_3** and **Ti:α-Fe_2O_3** photoanodes contained nanorod-like hematite blocks (Figure 1a–b). The presence of Ti on **Ti:α-Fe_2O_3** and copper on

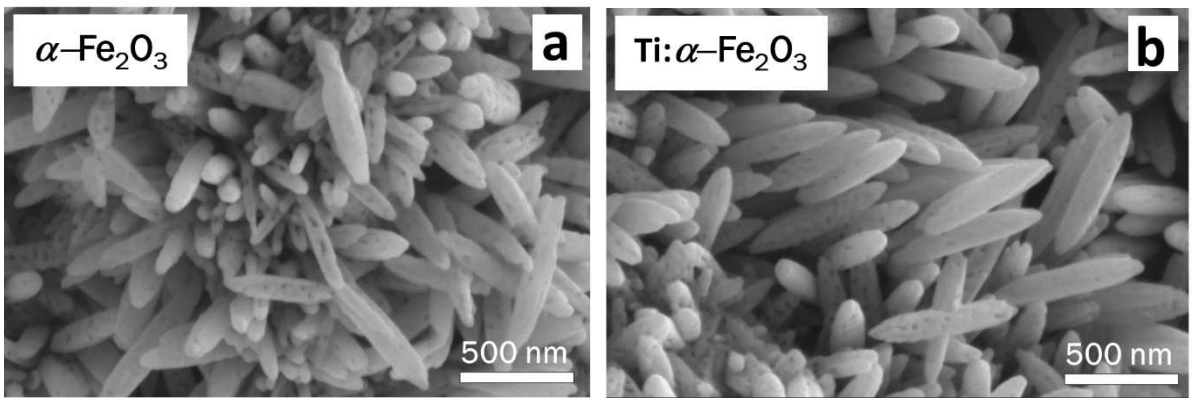

Figure 1. a–b) Top-view SEM images of the **α-Fe_2O_3** and **Ti:α-Fe_2O_3** photoanodes at ×50,000 magnification.

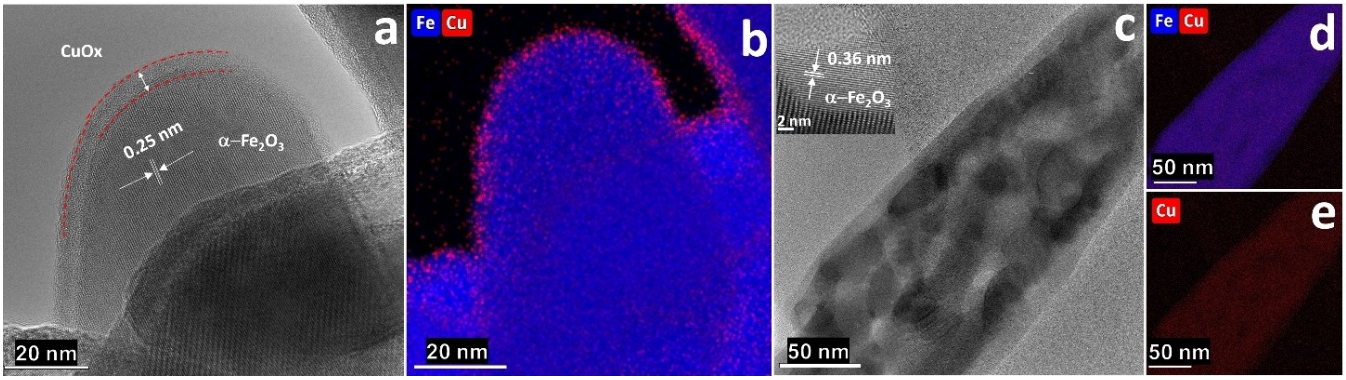

Figure 2. Side-view TEM images of the a) **CuOx/α-Fe_2O_3** and c) **CuOx/Ti:α-Fe_2O_3** photoanodes; and Cu and Fe elemental maps for b) **CuOx/α-Fe_2O_3** and d–e) **CuOx/Ti:α-Fe_2O_3** photoanodes.

the modified samples was confirmed by SEM-EDX, by scanning an extended area of the photoanodes (Figure S3–S4, Table S1), but no distinct surface structures related to copper-containing particles could be observed in the images.

Top-view SEM images showed that the length of the hematite nanorods was *ca.* 500 nm uniformly that was further confirmed by cross-sectional TEM (transmission electron microscopy) images. High-resolution transmission electron microscopy (HRTEM) image of the **CuOx/α-Fe_2O_3** and **CuOx/Ti:α-Fe_2O_3** shown in Figure 2a and c, revealed lattice periods of 0.25 nm and 0.36 nm referring to the (2–10) and (1–12) planes of hcp α-Fe_2O_3 structure, respectively. The diffraction peaks of all samples were in good agreement with those of hexagonal **α-Fe_2O_3** (ICSD 15840). The image of **CuOx/α-Fe_2O_3** (Figure 2a) also showed a *ca.* 3 nm-thick amorphous layer evenly distributed on the surface of the hematite nanorods, which was identified as Cu-containing layer by elemental mapping (Figure 2b). In Figure 2c, a hollow-like, porous structure of the Ti-doped hematite is seen, and the elemental maps show Cu distribution on the nanorods in a layer that is thinner than in **CuOx/α-Fe_2O_3** (Figure 2b). Due to the very thin coating on **CuOx/Ti:α-Fe_2O_3**, cross-sectional TEM images in this case were uninformative of the nature of CuOx. However, elemental mapping clearly showed the presence of Cu finely distributed on the surface of hematite rods (Figure 2d–e). Considering that we applied the same electrodeposition method and condition for the preparation of the CuOx ad-layer on the undoped and Ti-doped hematite, the differences in the features and the Cu-content of ad-layers on **CuOx/α-Fe_2O_3** and **CuOx/Ti:α-Fe_2O_3** result from the Ti-doping.

To further characterize the modified surfaces, we applied X-ray photoelectron spectroscopy (XPS). The XPS analysis of the photoanodes revealed the presence of B, C, Fe, O, and Ti on **α-Fe_2O_3** and **Ti:α-Fe_2O_3** samples and additionally, confirmed Cu on **CuOx/α-Fe_2O_3** and **CuOx/Ti:α-Fe_2O_3**. The surface composition of the photoanodes, detailed in Table 1, shows a difference in the amount of CuOx deposited on the undoped (3.4 at% Cu) and Ti-doped hematite samples (1.3 at% Cu), corroborating the TEM results.

In the case of **α-Fe_2O_3** and **Ti:α-Fe_2O_3** as well as the CuOx-modified samples, the binding energies (BEs) at 724.6 (Fe $2p_{1/2}$) and 711.2 eV (Fe $2p_{3/2}$) correspond to Fe^{3+} (Figure 3a).[63,64,65] In Figure 3b, we compared the Fe 2p spectra with known iron compounds, to confirm that our samples are indeed hematite and Ti-doping has no detectable influence on the chemical state of Fe, consistent with previous research on Ti-doped α-Fe_2O_3.[66] Similar O 1s spectra were measured for all photoanodes (Figure 3c), in which the peaks could be resolved into four components with BEs at 530.0 eV, 531.3 eV, 532.1 and 533.0 eV (Figure 3d shows the peak resolution for **CuOx/Ti:α-Fe_2O_3**). The first component corresponds to lattice oxygen species (O_L), and the second to the oxygen-deficient region (O_V). This includes various oxygen species (O^- or O_2^{2-}), hydroxyl groups (OH^-), and surface oxygen vacancies, which are saturated by hydroxyl groups due to adsorbed and deprotonated water on the oxide surface.[67–70] The third peak can be attributed to organic O species originated from the C–O compound of adventitious carbon.[65] The last peak, located at a higher energy, is associated with O_2 and/or H_2O molecules adsorbed on the surface.[71]

Distinct Ti 2p peaks at 458.4 eV ($2p_{3/2}$) and 464.1 eV ($2p_{1/2}$) are evident in all samples (Figure 3e), indicating that Ti is in a fully oxidized Ti^{4+} state. The surface atomic concentration of Ti was 5 times higher in the Ti-doped samples (1.5 at%); in **α-Fe_2O_3** and **CuOx/α-Fe_2O_3**, the 0.3 at% of Ti is due to the Ti substrate used for the fabrication of the photoanodes.

Table 1. Surface atomic concentrations (%) of the photoanodes calculated from XPS data.

	Surface atomic concentrations (%)			
	CuOx/α-Fe_2O_3	α-Fe_2O_3	CuOx/Ti:α-Fe_2O_3	Ti:α-Fe_2O_3
B 1s	0.8	1.2	0.6	0.7
C 1s	9.8	11.8	13.5	12.8
Cu 2p	3.4	0.0	1.3	0.0
Fe 2p	32.0	32.7	30.1	30.3
O 1s	53.6	54.0	53.2	54.7
Ti 2p	0.3	0.3	1.3	1.5

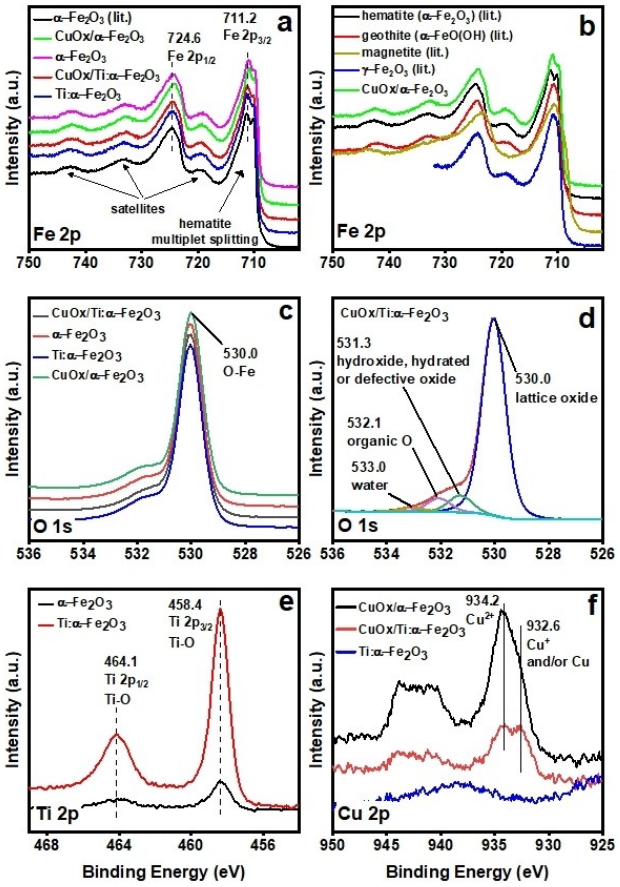

Figure 3. a) The Fe 2p XP spectra of the photoanodes; b) comparison of the Fe 2p binding energy region of **CuOx/Ti:α-Fe_2O_3** to literature (lit.) examples of different iron oxides and oxyhydroxides; c) the O 1s binding energy region of the samples; d) resolution of the O 1s peaks for **CuOx/Ti:α-Fe_2O_3**; e) comparison of the Ti 2p peaks of the **α-Fe_2O_3** and **Ti:α-Fe_2O_3** samples; and f) the Cu 2p peaks of the modified samples.

In the copper spectra (Figure 3f), binding energies located at 934.2 eV and 932.6 eV are attributed to Cu(II), Cu(I), and/or Cu(0) states, respectively. Notably, Cu(II) oxide and Cu(II)$(OH)_2$ species tend to decompose under X-ray irradiation and to a lesser extent under vacuum conditions. Consequently, the copper spectra were acquired at the onset of the measurement to minimize degradation and ensure data accuracy. The BEs show no difference between the undoped and the Ti-doped samples. However, there are differences in peak intensities, with the Ti-doped sample having a lower intensity, as indicated in Table 1. We have constructed a peak model for both samples as shown in Figure S5 and Figure S6). The Cu^{2+}:(Cu^{+}/Cu) ratio is roughly 5:1 in the **CuOx/α-Fe_2O_3** sample while the same ratio is roughly 2:1 in the **CuOx/Ti:α-Fe_2O_3** sample (see Table S2). We assume this difference relates to the lower copper content of the Ti-doped sample. The CuOx deposition on the Ti-doped sample was less efficient than on the undoped sample, despite using identical preparation methods and applying the same number of charges to prepare the **CuOx/α-Fe_2O_3** and **CuOx/Ti:α-Fe_2O_3** samples. Based on the fact, that the (Cu^{+}/Cu):Fe ratio remained the same, we assume a full copper surface coverage for both samples and a thicker layer on the **CuOx/α-Fe_2O_3** sample.

The combination of UV photoelectron spectroscopy (UPS) and inverse photoemission spectroscopy (IPES) provides us a direct method to measure the IE (ionization energy), EF (electron affinity), WF (work function) and Eg (transfer bandgap) of the surface (Figure S7–8). The electronic bandgap of the **Ti:α-Fe_2O_3** sample surface (Figure S7) was 2.1 eV with an error of +/−0.3 eV, which corresponds to the optical bandgap values of the samples measured by diffuse reflectance spectroscopy (DRS, Figure S9).

The combined morphological and surface composition analyses revealed that the electrodeposited CuOx layer is homogeneously and conformally distributed on the hematite and Ti-doped hematite nanorods in the form of an ad-layer, less than 3 nm-thick. The ad-layer is amorphous with a mixed Cu(II) and Cu(I) composition as expected from our previous study.[56] Thus, the CuOx was expected to act only as an optically inert (non-semiconducting) surface component in the system that was evidenced by DRS, showing the same optical band gap for each sample (Figure S9). To reveal the functional properties of CuOx, we conducted detailed electro- and photoelectrochemical studies that are discussed below.

Electrochemical Properties

The flat band potential (E_{Fb}) and the charge carrier density of the photoanodes were calculated by the Mott-Schottky plot (Figure S10). The E_{Fb} of hematite is reduced by Ti-doping, but the presence of CuOx is ineffective, either in **CuOx/α-Fe_2O_3** or **CuOx/Ti:α-Fe_2O_3** (Table 2), which is consistent with the unchanged onset potentials in the photocurrent–potential curves (*vide infra*). This indicates that CuOx leaves the interfacial energetics of the photoanodes unaffected.

The CuOx had only a minimal impact on the carrier density (N_d) of **α-Fe_2O_3** reducing it somewhat more in the case of **Ti:α-Fe_2O_3** (Table 2). Considering the small changes in the N_d values, almost all charges must be concentrated on hematite (or Ti-doped hematite), irrespective of the presence of CuOx under dark conditions. The double layer capacitance (C_{dl}) values for the photoanodes (Figure S11, Table 2) along with the derived electrochemically active surface area (ECSA) values, as a measure of surface reactivity at the electrode/electrolyte inter-

Table 2. Electrochemical properties of the photoanodes.

Photoanode	C_{dl} (μF)[a]	ECSA (cm^2)[b]	N_d (10^{19} cm^{-3})	E_{Fb} (V_{RHE})
Ti:α-Fe_2O_3	117	3.0	3.5	+0.62
CuOx/Ti:α-Fe_2O_3	91	2.3	2.3	+0.65
α-Fe_2O_3	97	2.4	2.8	+0.85
CuOx/α-Fe_2O_3	107	2.7	2.4	+0.86

[a] determined by cyclic voltammetry (CV) performed at different scan rates (v) in the non-Faradaic potential range (Figure S7). [b] derived from C_{dl} by using 40 μF cm^{-2} as the specific capacitance for flat **α-Fe_2O_3**.[72,73]

face during electrochemical reactions, have been also experimentally investigated. The lower C_{dl} and ECSA values for ***α*-Fe_2O_3** compared to **Ti:*α*-Fe_2O_3** (Table 2) are expected and coherent with the presence of the Ti-dopant. In the presence of CuOx, the C_{dl} values changed from 97 to 107 μF for ***α*-Fe_2O_3** and from 117 to 91 μF for the **Ti:*α*-Fe_2O_3**, suggesting that the presence of an ultrathin CuOx overlayer provides more electrochemically active sites for ***α*-Fe_2O_3**, while reducing their number in **Ti:*α*-Fe_2O_3**. Note that the differences in C_{dl} values are consistent with the results of photoelectrochemical (PEC) experiments (*vide infra*).

Photoelectrochemical Characterization of the Photoanodes

LSV (linear sweep voltammetry) experiments were performed under chopped irradiation, in a potential range of 0.6 to 1.9 V_{RHE}, using a three-electrode electrochemical cell (Figure 4a–b). Higher photocurrent density (*j*) was observed for **Ti:*α*-Fe_2O_3** compared to ***α*-Fe_2O_3** in the whole potential range; at 1.23 V_{RHE}, 0.26 and 0.37 mA/cm^2 for ***α*-Fe_2O_3** and for **Ti:*α*-Fe_2O_3**, respectively. The modification with CuOx improved *j* in the case of the pure ***α*-Fe_2O_3**, from 0.26 to 0.33 mA/cm^2, at 1.23 V_{RHE} and from 0.67 to 1.05 mA/cm^2 at 1.7 V_{RHE} (Figure 4a). In contrast, **CuOx/Ti:*α*-Fe_2O_3** exhibited a lower photocurrent (0.3 mA/cm^2 at 1.23 V_{RHE} and 0.8 mA/cm^2 at 1.7 V_{RHE}) than **Ti:*α*-Fe_2O_3** (0.37 and 1.0 mA/cm^2, respectively, Figure 4b). Similar trends were observed in strongly alkaline electrolyte (Figure S12). The charge separation and transport during the PEC oxidation reaction were studied in the presence of 0.5 M Na_2SO_3 hole scavenger. Figure 4c–d shows the charge separation (η_{cs}) and the charge transfer (η_{ct}) efficiencies of the photoanodes as a function of the applied potential. The η_{cs} slightly increased in the potential range of 0.7 V_{RHE} to 1.3 V_{RHE} by CuOx modification, in both pure ***α*-Fe_2O_3** and **Ti:*α*-Fe_2O_3** photoanodes and reached a maximum of 40.5% in ***α*-Fe_2O_3** which means that the CuOx suppressed the bulk recombination process in hematite. The effect of CuOx on η_{ct} correlates with the photocurrent density.

The increased photocurrent observed with **Ti:*α*-Fe_2O_3** compared to the pure ***α*-Fe_2O_3** can be attributed to the higher η_{ct}. In this case, the higher *j* but lower η_{cs} means more efficient charge injection to the electrolyte, *i.e.*, the rate of charge transfer prevails that of bulk recombination. In ***α*-Fe_2O_3**, CuOx increased η_{ct}, from 21% to 32% at 1.7 V_{RHE} indicating a decrease in electron-hole recombination at the surface. Conversely, CuOx on **Ti:*α*-Fe_2O_3** reduced the η_{ct} from 42% to 34% at the same potential.

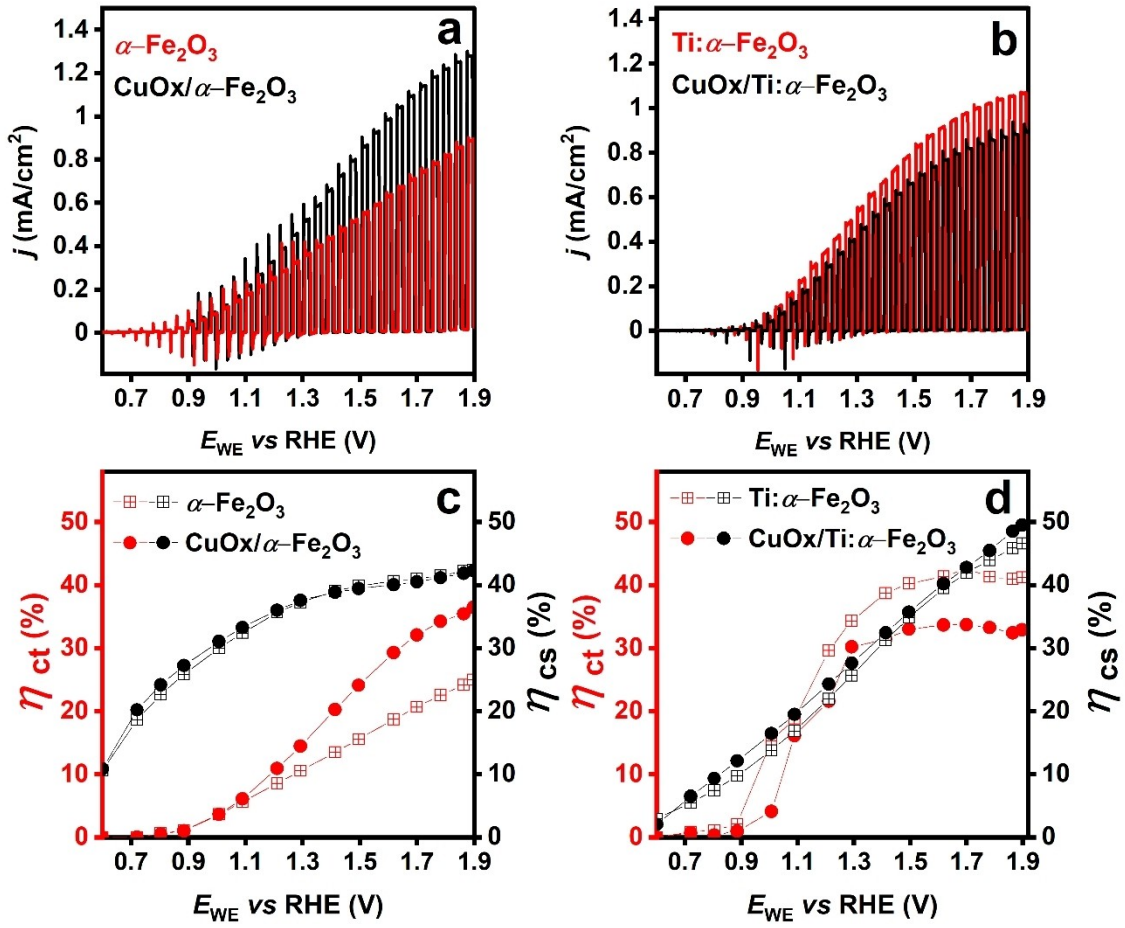

Figure 4. a–b) Linear sweep voltammetry plots of the photoanodes obtained in 0.1 M borate buffer at pH 9.2, under chopped irradiation with 100 mW/cm^2, ν = 2 mV/s, Pt aux. and Ag/AgCl ref.); c–d) charge separation (η_{cs}) and charge transfer (η_{ct}) efficiency of the photoanodes.

To elucidate the reasons for the opposite response of α-Fe_2O_3 and Ti:α-Fe_2O_3 upon CuOx, we performed potentiostatic electrochemical impedance spectroscopy (PEIS) at potentials covering the surface states, since this method is widely accepted to study the charge dynamics within photoelectrodes. Interfacial charge transfer for water oxidation on hematite is associated with the surface states S1 (higher in energy) and S2 (lower in energy). Although the exact overall mechanism is a matter of debate, it is generally accepted that S1 is involved directly in the rate-limiting O–O bond formation step.[74] Co-catalysts can effectively compete with the surface states by providing alternative pathways for charge transfer or opening new sites for the chemical steps.

As for our hematite samples, the equivalent circuit fitting of the experimental PEIS data was based on the two observed semicircles in the Nyquist plots (Figure S13), representing the hole migration from the bulk to the surface and then, to surface reactions. The derived charge transfer capacitance (C_{SS}) is the overall value contributed by all surface states, and it is not possible to distinguish the contribution of the individual charge transfer processes. The fitted surface state capacitances as a function of the applied potential are shown in Figure 5a–b. For α-Fe_2O_3, the potential-dependent C_{SS} exhibited two peaks indicating the existence of S1 and S2 located at 1.3 V and 0.7 V_{RHE}, respectively, in line with previous studies.[2,6,26,28,74] At the potential of S2, the R_{ct} (charge transfer resistance) shows a characteristic peak (Figure S14a), which indicates that charge transfer is unfavored through S2 in pure hematite, and the recombination process dominates, since no photocurrent is observed at this potential. For Ti:α-Fe_2O_3, the potential dependence of C_{SS} exhibited only one peak located at 1.0 V_{RHE} assigned to S1. In this case, the favored charge transfer *via* S1 is clearly indicated by the drop in R_{ct} (Figure S14b). The absence of a second peak shows that the introduction of Ti-doping into hematite leads to the elimination of the S2 state and a higher photocurrent density when compared to α-Fe_2O_3. Importantly, as efficiency data in Figure 4c–d suggest, the effect of Ti-doping is manifested in a higher charge transfer efficiency compared to pristine hematite. This means that the Ti-doping increases the water splitting activity on the surface, which can be correlated with S1 surface states.

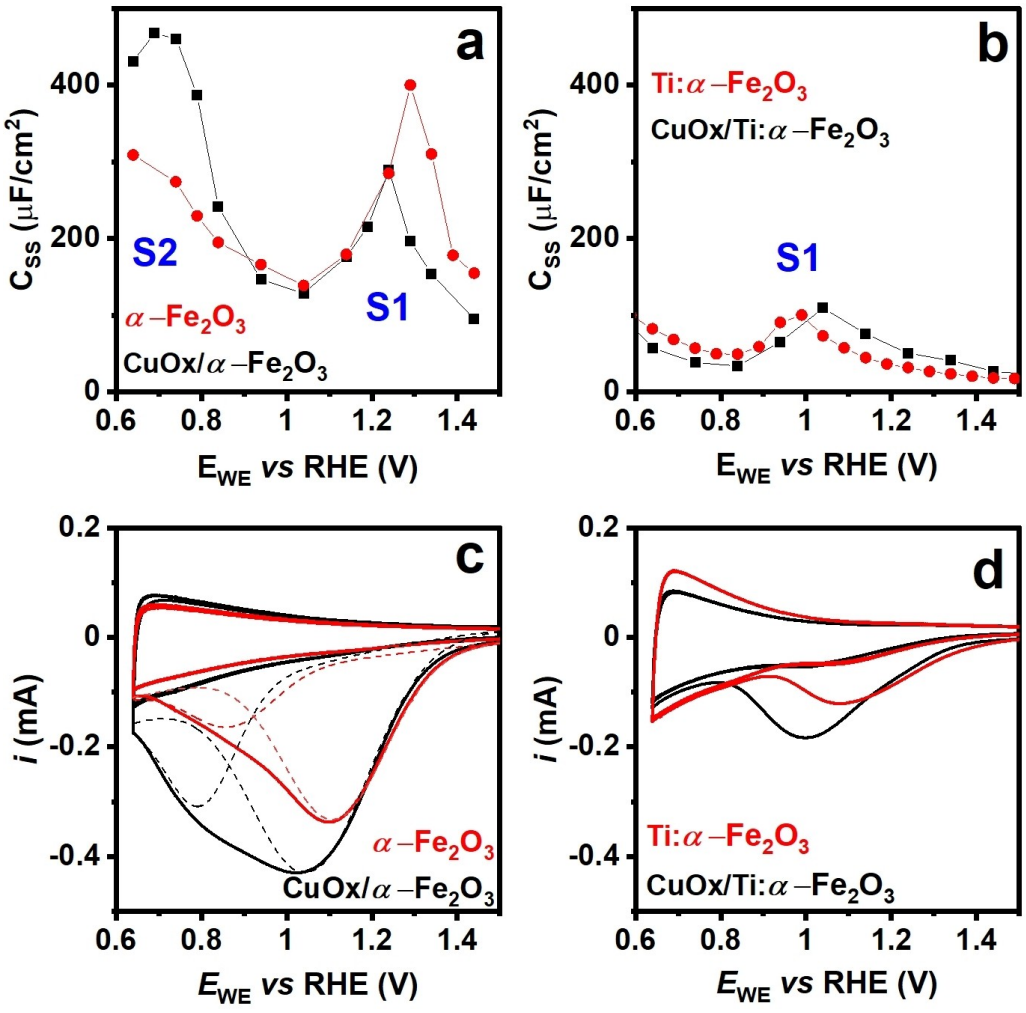

Figure 5. a–b) Surface state capacitances (C_{SS}) of the photoanodes extracted from EIS under irradiation with 100 mW/cm^2; c–d) fast cathodic CV curves of the photoanodes after holding the electrodes at 1.64 V_{RHE} under irradiation for 1 min, W = 100 mW/cm^2, ν = 200 mV/s.

For **CuOx/α-Fe_2O_3**, the change in C_{SS} with the external bias shows that S1 is shifted to lower potentials and S2 is described by a nearly 2 times higher C_{SS} value than **α-Fe_2O_3**, which means that the holes at the surface are accumulated in the S2 state.[75] In contrast, for **CuOx/Ti:α-Fe_2O_3**, a small anodic shift can be observed in the potential for S1.

To further characterize the dynamics of surface states, holes were accumulated on the surface under irradiation for 1 minute, at high external bias, followed by a fast cathodic CV scan in the dark (Figure 5c–d). The observations correlated with the results of the PEIS experiments: in **α-Fe_2O_3**, two overlapping cathodic current waves were identified in the first CV scan, corresponding to the electron fill of photogenerated S1 and S2 (Figure 5c). The current completely decayed after the initial scan, indicating the consumption of photogenerated holes. In **Ti:α-Fe_2O_3**, one cathodic peak could be observed corresponding to S1 (Figure 5d). Modification of the photoanodes with CuOx resulted in similar CV features assigned as S1 and S2 for **CuOx/α-Fe_2O_3**, and S1 for **CuOx/Ti:α-Fe_2O_3**, and a slight shift of the peaks to lower potentials.

Our findings indicate that CuOx has a potential-dependent role that is related to the presence of the different surface states on **α-Fe_2O_3**.[26] It is generally accepted in literature that in pure **α-Fe_2O_3** there are two energetically separated surface states, S2 lower and S1 higher in energy (Scheme 1a). However, their energy and density may differ that has been attributed to multiple reasons such as differences in sample preparation methods, post treatments and test conditions.[2] Thus, the nature and chemical identity of surface states are maybe not always the same, making it hard to define general physical parameters. Therefore, our conclusions about the role of CuOx on pure hematite – while indicative – may not be generalized directly to other examples.

Specifically, in the potential region where the photocurrent is very low, and R_{ct} indicates unfavorable charge transfer, CuOx functions as a hole reservoir in equilibrium with S2. It collects holes but exhibits poor transferability to advance the OER, due to the insufficient – most likely isolated – formation of oxidized Cu sites.[76] This behavior changes in the higher anodic potential regime ($>1.1\ V_{RHE}$), where CuOx acts as co-catalyst and thus suppresses surface recombination in hematite, as evidenced by the increased photocurrent and η_{ct} of **CuOx/α-Fe_2O_3** (Scheme 1a–b).

In **CuOx/Ti:α-Fe_2O_3**, the deposition of CuOx was inherently less efficient and S2 was missing from **Ti:α-Fe_2O_3**, in contrast with **CuOx/α-Fe_2O_3**. As for **Ti:α-Fe_2O_3** with no CuOx coating, at moderate potentials, Ti doping compromises charge separation efficiency in **Ti:α-Fe_2O_3** compared to **α-Fe_2O_3** (Figure 4c–d), but the lower flat-band potential provides higher thermodynamic driving force to increase the photocurrent. With the increasing external bias, the photocurrent becomes higher due to the Ti-dopant that lowers the potential of S1 and enhances η_{ct} compared to the undoped hematite.

Importantly, CuOx reduces the photocurrent on **CuOx/Ti:α-Fe_2O_3** relative to **Ti:α-Fe_2O_3** in the whole potential range. The adverse effect of CuOx can be associated with the reduced η_{ct} (Figure 4d) indicating blocked S1 active sites. The key to understand the sharp difference in the behavior of CuOx on **α-Fe_2O_3** and **Ti:α-Fe_2O_3** is the missing S2 state in the latter (Scheme 1c–d). With the experimental findings in mind, one can conclude that CuOx can accept holes only from S2, while cannot do so from S1 that explains its co-catalytic effect on **α-Fe_2O_3** and the S1 blocking effect on **Ti:α-Fe_2O_3**. In this context, the presence of S2 in hematite is crucial to activate the CuOx co-catalyst layer on the surface.

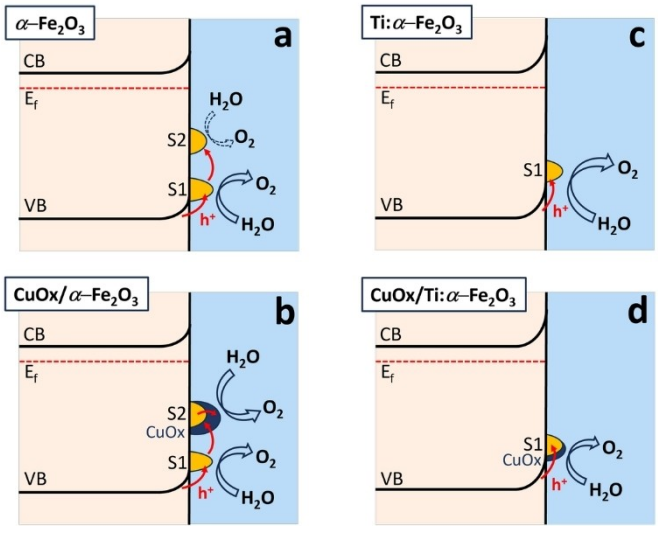

Scheme 1. Schematic representation of the charge transfer processes in the a) **CuOx/α-Fe_2O_3** and b) **CuOx/Ti:α-Fe_2O_3** photoanodes.

Conclusions

An amorphous thin layer of a mixture of cupric and cuprous oxyhydroxide (CuOx co-catalyst) has been electrodeposited onto pristine and Ti-doped, isomorphous hematite photoanodes to boost the oxygen evolving reaction (OER). Our results imply that the mediation of hematite surface states is crucial for the successful transfer of valence band holes to the CuOx surface co-catalyst. In the absence of such a charge transfer pathway, the CuOx remains a passive component, blocking the intrinsic reactivity of the photoexcited hematite in the OER. Specifically, in pristine **α-Fe_2O_3** the introduction of CuOx has a potential-dependent, positive impact on the performance. At lower potential, corresponding to S2, CuOx serves as hole reservoir, collecting but not utilizing holes for the OER, due to the insufficient formation of oxidized Cu sites. At higher potentials, CuOx suppresses surface recombination, and acts as co-catalyst. In **Ti:α-Fe_2O_3** where the S2 state is absent, CuOx rather blocks the S1 sites that are intrinsically more active than those in **α-Fe_2O_3** (note that despite identical conditions, the deposition of CuOx itself was less effective on **Ti:α-Fe_2O_3**). Our work underlines that the design of co-catalyst/semiconductor combinations may result ineffective systems without knowing the actual nature and accessibility of surface states to the co-catalyst. On the other hand, effective co-catalyst electrodeposition may in itself imply that surface states capable of trans-

ferring charges to the co-catalyst exist and will support an efficient catalytic reaction.

Supporting Information

The authors have cited additional references within the Supporting Information.[77–84]

Acknowledgements

The authors are grateful to Noémi Szász for the preparation of the TEM samples. This work was supported by the National Research, Development and Innovation (NRDI) Fund of Hungary (Hungary); grant numbers NKFI-128841 and TKP2021-NKTA-05, and National Natural Science Foundation of China (Grant No. 52225606). This research was supported by the grant no. VEKOP-2.3.3-15-2016-00002 and VEKOP-2.3.2-16-2016-00011 of the European Structural and Investment Funds. We also thank the Renewable Energy National Laboratory (Hungary) for support, financed by the RRF-2.3.1-21-2022-00009 project.

Conflict of Interests

The authors declare no conflict of interest.

Data Availability Statement

The data that support the findings of this study are available from the corresponding author upon reasonable request.

Keywords: copper-oxide · hematite · nanostructures · semiconductors · water splitting

[1] L. Mao, Y.-C. Huang, H. Deng, F. Meng, Y. Fu, Y. Wang, M. Li, Q. Zhang, C.-L. Dong, L. Gu, S. Shen, *Small* **2023**, *19*, 2203838.
[2] J. Li, H. Chen, C. A. Triana, G. R. Patzke, *Angew. Chem. Int. Ed.* **2021**, *60*, 18380–18396.
[3] A. G. Tamirat, J. Rick, A. A. Dubale, W.-N. Su, B.-J. Hwang, *Nanoscale Horiz.* **2016**, *1*, 243–267.
[4] C. Lohaus, *The Fermi Level in Hematite - Doping, Band Alignment, and Charge Transitions*, Ph.D. Tesis, Technical University of Darmstadt, **2019**.
[5] J. Ma, Q. Wang, L. Li, X. Zong, H. Sun, R. Tao, X. Fan, *J. Colloid Interface Sci.* **2021**, *602*, 32–42.
[6] J. Li, W. Wan, C. A. Triana, Z. Novotny, J. Osterwalder, R. Erni, G. R. Patzke, *J. Am. Chem. Soc.* **2019**, *141*, 12839–12848.
[7] S. Shen, J. Zhou, C.-L. Dong, Y. Hu, E. N. Tseng, P. Guo, L. Guo, S. S. Mao, *Sci. Rep.* **2014**, *4*, 6627.
[8] C. Liu, T. Zhang, D. Zhao, C. Zhang, G. Ou, H. Jin, Z. Chen, *J. Mater. Sci. Mater. Electron.* **2021**, *32*, 7061–7072.
[9] J.-C. Chou, S.-A. Lin, C.-Y. Lee, J.-Y. Gan, *J. Mater. Chem. A* **2013**, *1*, 5908–5914.
[10] S. Tanaka, Y. V. Kaneti, N. L. W. Septiani, S. X. Dou, Y. Bando, Md. S. A. Hossain, J. Kim, Y. Yamauchi, *Small Methods* **2019**, *3*, 1800512.
[11] G. T. Dos Santos, K. C. Bedin, T. E. R. Fiuza, I. Rodríguez-Gutiérrez, P. F. P. Fichtner, F. L. Souza, J. Bettini, *Appl. Surf. Sci.* **2024**, *645*, 158867.
[12] N. C. Verissimo, F. A. Pires, I. Rodriguez-Gutierrez, J. Bettini, T. E. E. R. Fiuza, C. Alexandre Biffe, F. Montoro, G. Ravanhani Schleder, R. HR. Castro, E. Roberto Leite, F. Leandro Souza, *J. Mater. Chem. A* **2024**, DOI 10.1039/D3TA07721G.
[13] B. R. Lima, I. Rodriguez-Gutierrez, N. C. Verissimo, Â. Albuquerque, G. T. Santos, J. Bettini, F. L. Souza, *Mater. Today Chem.* **2023**, *34*, 101784.
[14] K. T. C. Thomaz, K. C. Bedin, I. Rodríguez-Gutiérrez, N. C. Verissimo, J. Bettini, F. L. Souza, *Mater. Today Energy* **2023**, *37*, 101399.
[15] F. A. Pires, G. T. dos Santos, J. Bettini, C. A. R. Costa, R. V. Gonçalves, R. H. R. Castro, F. L. Souza, *Sustain. Energy Fuels* **2023**, *7*, 5005–5017.
[16] J. B. Souza Junior, F. L. Souza, L. Vayssieres, O. K. Varghese, *Appl. Phys. Lett.* **2021**, *119*, 200501.
[17] I. Rodriguez-Gutierrez, J. B. Souza Junior, E. R. Leite, L. Vayssieres, F. L. Souza, *Appl. Phys. Lett.* **2021**, *119*, 071602.
[18] X. Guan, S. Zong, S. Shen, *Nano Res.* **2022**, *15*, 10171–10184.
[19] A. Tofanello, Z. Diao, E. Djatoubai, J. Z. Su, S. H. Shen, F. L. Souza, L. Vayssieres, *J. Appl. Phys.* **2020**, *128*, 063103.
[20] F. Niu, D. Wang, F. Li, Y. Liu, S. Shen, T. J. Meyer, *Adv. Energy Mater.* **2020**, *10*, 1900399.
[21] Y. Fu, Y.-R. Lu, F. Ren, Z. Xing, J. Chen, P. Guo, W.-F. Pong, C.-L. Dong, L. Zhao, S. Shen, *Solar RRL* **2020**, *4*, 1900349.
[22] L. Mao, Y.-C. Huang, Y. Fu, C.-L. Dong, S. Shen, *Sci. Bull.* **2019**, *64*, 1262–1271.
[23] X. Chen, Y. Fu, T. Kong, Y. Shang, F. Niu, Z. Diao, S. Shen, *Eur. J. Inorg. Chem.* **2019**, *2019*, 2078–2085.
[24] J. Su, L. Vayssieres, *ACS Energy Lett.* **2016**, *1*, 121–135.
[25] B. Iandolo, B. Wickman, I. Zorić, A. Hellman, *J. Mater. Chem. A* **2015**, *3*, 16896–16912.
[26] Z. Pan, S. Chen, K. Katayama, *J. Phys. Chem. C* **2023**, *127*, 3904–3909.
[27] O. Zandi, T. W. Hamann, *J. Phys. Chem. Lett.* **2014**, *5*, 1522–1526.
[28] B. Iandolo, A. Hellman, *Angew. Chem. Int. Ed.* **2014**, *53*, 13404–13408.
[29] A. Tofanello, S. Shen, F. L. de Souza, L. Vayssieres, *APL Mater.* **2020**, *8*, 040905.
[30] A. M. S. Santos, I. Rodríguez-Gutiérrez, G. M. Morishita, R. M. Lopes, F. L. Souza, *Mater. Lett.* **2024**, *357*, 135781.
[31] Y. Chen, F. Lv, H. Xia, X. Xu, J. Su, S. Shen, *Appl. Phys. Lett.* **2021**, *119*, 083901.
[32] C. X. Kronawitter, I. Zegkinoglou, S.-H. Shen, P. Liao, I. S. Cho, O. Zandi, Y.-S. Liu, K. Lashgari, G. Westin, J.-H. Guo, F. J. Himpsel, E. A. Carter, X. L. Zheng, T. W. Hamann, B. E. Koel, S. S. Mao, L. Vayssieres, *Energy Env. Sci* **2014**, *7*, 3100–3121.
[33] D. Stanescu, M. Piriyev, V. Villard, C. Mocuta, A. Besson, D. Ihiawakrim, O. Ersen, J. Leroy, S. G. Chiuzbaian, A. P. Hitchcock, S. Stanescu, *J. Mater. Chem. A* **2020**, *8*, 20513–20530.
[34] L. Badia-Bou, E. Mas-Marza, P. Rodenas, E. M. Barea, F. Fabregat-Santiago, S. Gimenez, E. Peris, J. Bisquert, *J. Phys. Chem. C* **2013**, *117*(8), 3826–3833.
[35] S. D. Tilley, M. Cornuz, K. Sivula, M. Grätzel, *Angew. Chem. Int. Ed.* **2010**, *49*, 6405–6408.
[36] M. Barroso, A. J. Cowan, S. R. Pendlebury, M. Grätzel, D. R. Klug, J. R. Durrant, *J. Am. Chem. Soc.* **2011**, *133*, 14868–14871.
[37] G. M. Carroll, D. R. Gamelin, *J. Mater. Chem. A* **2016**, *4*, 2986–2994.
[38] B. Klahr, S. Gimenez, F. Fabregat-Santiago, J. Bisquert, T. W. Hamann, *J. Am. Chem. Soc.* **2012**, *134*, 16693–16700.
[39] D. K. Zhong, D. R. Gamelin, *J. Am. Chem. Soc.* **2010**, *132*, 4202–4207.
[40] K. J. McDonald, K.-S. Choi, *Chem. Mater.* **2011**, *23*, 1686–1693.
[41] B. Eftekharinia, A. Moshaii, A. Dabirian, N. S. Vayghan, *J. Mater. Chem. A* **2017**, *5*, 3412–3424.
[42] M. Barroso, C. A. Mesa, S. R. Pendlebury, A. J. Cowan, T. Hisatomi, K. Sivula, M. Grätzel, D. R. Klug, J. R. Durrant, *Proc. Nat. Acad. Sci.* **2012**, *109*, 15640–15645.
[43] X. Chen, Y. Fu, L. Hong, T. Kong, X. Shi, G. Wang, L. Qu, S. Shen, *J. Chem. Phys.* **2020**, *152*, 244707.
[44] C. Li, S. Ma, M. Zhao, M. Jing, W. Yuan, C. Li, *ACS Sustainable Chem. Eng.* **2023**, *11*, 12102–12113.
[45] C. Li, Z. Chen, W. Yuan, Q.-H. Xu, C. M. Li, *Nanoscale* **2019**, *11*, 1111–1122.
[46] N. Dalle Carbonare, V. Cristino, S. Berardi, S. Carli, R. Argazzi, S. Caramori, L. Meda, A. Tacca, C. A. Bignozzi, *ChemPhysChem* **2014**, *15*, 1164–1174.
[47] T. Wang, X. Long, S. Wei, P. Wang, C. Wang, J. Jin, G. Hu, *ACS Appl. Mater. Interfaces* **2020**, *12*, 49705–49712.
[48] J. E. Thorne, J.-W. Jang, E. Y. Liu, D. Wang, *Chem. Sci.* **2016**, *7*, 3347–3354.
[49] K. C. Bedin, I. Rodríguez-Gutiérrez, L. R. P. Peregrino, L. Vayssieres, F. L. Souza, *J. Am. Ceram. Soc.* **2023**, *106*, 79–92.
[50] J. Zhang, R. García-Rodríguez, P. Cameron, S. Eslava, *Energy Environ. Sci.* **2018**, *11*, 2972–2984.

[51] F. Yu, F. Li, B. Zhang, H. Li, L. Sun, *ACS Catal.* **2015**, *5*, 627–630.
[52] X. Liu, S. Cui, M. Qian, Z. Sun, P. Du, *Chem. Commun.* **2016**, *52*, 5546–5549.
[53] K. J. Fisher, K. L. Materna, B. Q. Mercado, R. H. Crabtree, G. W. Brudvig, *ACS Catal.* **2017**, *7*, 3384–3387.
[54] E. C. Pastrana, V. Zamora, D. Wang, H. Alarcón, *Adv. Nat. Sci. Nanosci. Nanotechnol.* **2019**, *10*, 035012.
[55] P. I. Kyesmen, N. Nombona, M. Diale, *J. Alloys Compd.* **2021**, *863*, 158724.
[56] D. Lukács, M. Németh, Ł. Szyrwiel, L. Illés, B. Pécz, S. Shen, J. S. Pap, *Sol. Energy Mater. Sol. Cells* **2019**, *201*, 110079.
[57] S. Shen, S. A. Lindley, X. Chen, J. Z. Zhang, *Energy Environ. Sci.* **2016**, *9*, 2744–2775.
[58] K. C. Bedin, D. N. F. Muche, M. A. Melo Jr, A. L. M. Freitas, R. V. Gonçalves, F. L. Souza, *ChemCatChem* **2020**, *12*, 3156–3169.
[59] X. Wan, L. Wang, C.-L. Dong, G. Menendez Rodriguez, Y.-C. Huang, A. Macchioni, S. Shen, *ACS Energy Lett.* **2018**, *3*, 1613–1619.
[60] L. Vayssieres, N. Beermann, S.-E. Lindquist, A. Hagfeldt, *Chem. Mater.* **2001**, *13*, 233–235.
[61] V. A. N. de Carvalho, R. A. de S Luz, B. H. Lima, F. N. Crespilho, E. R. Leite, F. L. Souza, *J. Power Sources* **2012**, *205*, 525–529.
[62] J. S. Pap, A. Draksharapu, M. Giorgi, W. R. Browne, J. Kaizer, G. Speier, *Chem. Commun.* **2014**, *50*, 1326–1329.
[63] S. M. Al-Zuraiji, T. Benkó, L. Illés, M. Németh, K. Frey, A. Sulyok, J. S. Pap, *J. Catal.* **2020**, *381*, 615–625.
[64] M. C. Biesinger, B. P. Payne, A. P. Grosvenor, L. W. M. Lau, A. R. Gerson, R. St C Smart, *Appl. Surf. Sci.* **2011**, *257*, 2717–2730.
[65] B. V. Crist, *Handbook of Monochromatic XPS Spectra, The Elements of Native Oxides*, Wiley, Chichester, New York, **2000**.
[66] S. Shen, C. X. Kronawitter, D. A. Wheeler, P. Guo, S. A. Lindley, J. Jiang, J. Z. Zhang, L. Guo, S. S. Mao, *J. Mater. Chem. A* **2013**, *1*, 14498–14506.
[67] T. J. Frankcombe, Y. Liu, *Chem. Mater.* **2023**, *35*, 5468–5474.
[68] N. P. Prasad, M. Rohnke, M. A. Verheijen, J. M. Sturm, J. P. Hofmann, E. J. M. Hensen, A. Bieberle-Hütter, *ACS Appl. Energ. Mater.* **2023**, *6*, 12237–12248.
[69] D. J. Morgan, *Surf. Interface Anal.* **2023**, *55*, 845–850.
[70] H. Idriss, *Surf. Sci.* **2021**, *712*, 121894.
[71] T. Benkó, S. Shen, M. Németh, J. Su, Á. Szamosvölgyi, Z. Kovács, G. Sáfrán, S. M. Al-Zuraiji, E. Z. Horváth, A. Sápi, Z. Kónya, J. S. Pap, *Appl. Catal. Gen.* **2023**, *652*, 119035.
[72] L. Mao, H. Deng, M. Li, S. Shen, *Sci. China Mater.* **2023**, *66*, 603–613.
[73] Q. Chen, Y. Chong, M. Rao, M. Su, Y. Qiu, *Processes* **2021**, *9*, 1102.
[74] J. Li, W. Wan, C. A. Triana, H. Chen, Y. Zhao, C. K. Mavrokefalos, G. R. Patzke, *Nat. Commun.* **2021**, *12*, 255.
[75] B. Klahr, S. Gimenez, O. Zandi, F. Fabregat-Santiago, T. Hamann, *ACS Appl. Mater. Interfaces* **2015**, *7*, 7653–7660.
[76] Y. Dai, P. Cheng, G. Xie, C. Li, M. Z. Akram, B. Guo, R. Boddula, X. Shi, J. Gong, J. R. Gong, *J. Phys. Chem. C* **2019**, *123*, 28753–28762.
[77] C. Heske, *Characterization of the Electronic and Chemical Structure at the Thin Film Solar Cell Interfaces: June 2005–June 2009*, University of Nevada, Las Vegas, Nevada, **2009**.
[78] J. Carter, *Chemical and Electronic Surface Structure of Chalcopyrite-Based Thin Films for Solar Water Splitting* **2020**, UNLV Theses Diss. Prof. Pap. Capstones 3872, DOI 10.34917/19412030.
[79] R. F. Duarte, *Analysis and Optimization of Interfaces in "Wide Gap" Chalcopyrite based Thin Film Solar Cell Devices*, PhD thesis, Brandenburg University of Technology, **2015**.
[80] L. Weinhardt, O. Fuchs, D. Groß, G. Storch, E. Umbach, N. G. Dhere, A. A. Kadam, S. S. Kulkarni, C. Heske, *Appl. Phys. Lett.* **2005**, *86*, 062109.
[81] C. Lohaus, C. Steinert, J. Brötz, A. Klein, W. Jaegermann, *Adv. Mater. Interfaces* **2017**, *4*, 1700542.
[82] J. Engel, H. L. Tuller, *Phys. Chem. Chem. Phys.* **2014**, *16*, 11374–11380.
[83] J. A. Glasscock, P. R. F. Barnes, I. C. Plumb, A. Bendavid, P. J. Martin, *Thin Solid Films* **2008**, *516*, 1716–1724.
[84] L. A. Marusak, R. Messier, W. B. White, *J. Phys. Chem. Solids* **1980**, *41*, 981–984.

Manuscript received: February 27, 2024
Revised manuscript received: April 20, 2024
Version of record online: June 17, 2024